

Planar heterostructures of single-layer transition metal dichalcogenides: Composite structures, Schottky junctions, tunneling barriers, and half metals

Mehmet Aras and Çetin Kılıç*

Department of Physics, Gebze Technical University, 41400 Kocaeli, Turkey

S. Ciraci†

Department of Physics, Bilkent University, 06800 Ankara, Turkey

(Received 28 July 2016; revised manuscript received 29 January 2017; published 28 February 2017)

Planar composite structures formed from the stripes of transition metal dichalcogenides joined commensurately along their zigzag or armchair edges can attain different states in a two-dimensional (2D), single-layer, such as a half metal, 2D or one-dimensional (1D) nonmagnetic metal and semiconductor. Widening of stripes induces metal-insulator transition through the confinements of electronic states to adjacent stripes, that results in the metal-semiconductor junction with a well-defined band lineup. Linear bending of the band edges of the semiconductor to form a Schottky barrier at the boundary between the metal and semiconductor is revealed. Unexpectedly, strictly 1D metallic states develop in a 2D system along the boundaries between stripes, which pins the Fermi level. Through the δ doping of a narrow metallic stripe one attains a nanowire in the 2D semiconducting sheet or narrow band semiconductor. A diverse combination of constituent stripes in either periodically repeating or finite-size heterostructures can acquire critical fundamental features and offer device capacities, such as Schottky junctions, nanocapacitors, resonant tunneling double barriers, and spin valves. These predictions are obtained from first-principles calculations performed in the framework of density functional theory.

DOI: [10.1103/PhysRevB.95.075434](https://doi.org/10.1103/PhysRevB.95.075434)

I. INTRODUCTION

Single- and multilayer transition metal dichalcogenides have started to dominate the research on two-dimensional (2D) materials [1–7]. Already the stability of similar single-layer hexagonal and trigonal (H and T) structures of several transition metal oxides and dichalcogenides has been predicted [8]. Unusual electronic properties and important device capacities thereof have been heralded by early theoretical studies on planar or in-plane heterostructures of nanoribbons [9,10]. Much recently, the realization of vertical van der Waals solids [11,12], as well as lateral, in-plane heterostructures of single-layer (SL) transition metal dichalcogenides TMD [13–16], have opened an active field of experimental and theoretical research.

In this paper, we show that periodically repeating, commensurate junctions of nanoribbons (stripes) forming SL in-plane *composite structures*, $(\text{MoTe}_2)_p/(\text{NiTe}_2)_q$ (specified in the text as S_p/M_q with p and q being the numbers of formula units) constitute a class of materials offering crucial fundamental features and diverse device applications. Since both 2D constituents have been synthesized already [17], earlier growth studies [14,18,19] and present theoretical analysis of energetics and stability let us expect that these SL composite structures with sharp boundaries can readily be produced [20–24] and remain stable in diverse applications.

Various combinations of p and q starting from $p = 2$ and $q = 2$ result in composite materials with tunable properties such as metal, narrow band gap semiconductor and metal semiconductor as well as metal-magnetic metal junctions. The δ doping corresponding to $q = 2$ but $p \gg 2$ forms

strictly one-dimensional (1D) metals (or nanowires) in a 2D semiconductor. For large S and M stripes corresponding to $p \gg 1$ and $q \gg 1$, electronic states become confined so that they attain the properties of their parent 2D constituents, but the charge is transferred across the 1D boundaries between them. Eventually, an asymmetric Schottky barrier of significant height is constructed together with strictly 1D metallic states propagating at the boundaries in a 2D single-layer structure. Since impurities are absent at the boundaries, linear bending of the band edges near the boundaries are attained.

A composite with finite width made by commensurately joined $M_q - S_p - M_q$ stripes and capped by vacuum from both sides can form a nanocapacitor or a tunneling barrier (or a resonant tunneling double barrier through a combination $M_q - S_p - S'_t - S_p - M_q$). Alternatively, a composite structure constructed by the junction of magnetic metal-nonmagnetic metal, $(\text{FeTe}_2)_t/(\text{NiTe}_2)_q$ (i.e., mM_t/M_q) display half metallic properties and can operate as a spin valve. Notably, most of the fundamental features revealed in these composite structures are not sensitive to the specific values of structural parameters p , q , and t ; they require only wide enough stripes allowing localization.

II. METHOD

Our predictions in this paper were obtained from first-principles calculations based on the density functional theory (DFT), which were carried out using the VIENNA *ab initio* simulation package [25]. These calculations were performed within the local spin density approximation (LSDA) using the Ceperley-Alder (CA) exchange-correlation functional [26]. We employed the projector augmented-wave (PAW) method [27,28], treating the $3d$ and $4s$, $3d$, and $4s$, $4d$ and $5s$, and $5p$ states as valence states for iron, nickel, molybdenum,

*cetin_kilic@gtu.edu.tr

†ciraci@fen.bilkent.edu.tr

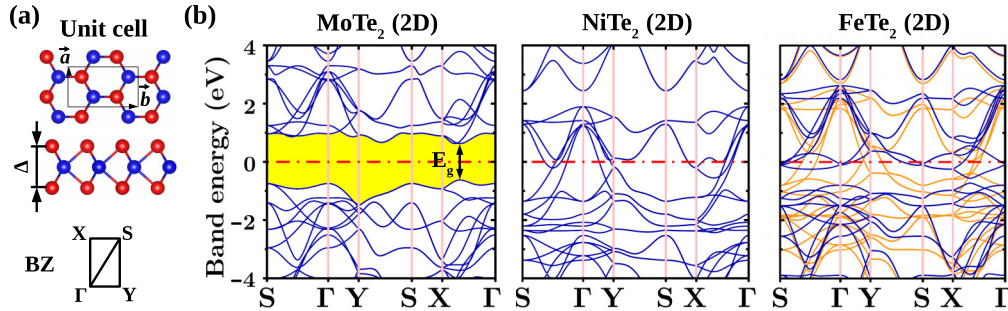


FIG. 1. (a) Top and side views of the optimized atomic structure of 2D SL transition metal dichalcogenides, MoTe₂, NiTe₂, and FeTe₂. The layer thickness is denoted by Δ . The rectangular unit cell is delineated and has lattice constants a and b . (b) The electronic energy bands are calculated within the LSDA using the optimized atomic structures. The zero of energy of the semiconducting MoTe₂ is set at its intrinsic Fermi level.

and tellurium, respectively. Plane wave basis sets were used to represent the electronic states, which were determined by imposing a kinetic energy cutoff of 400 eV (in geometry optimizations as well as band-structure and DOS calculations) or 300 eV (in molecular dynamics simulations). Convergence criterion for the electronic self-consistency was set up to 10^{-6} eV. An orthorhombic supercell with adequate dimensions was devised for each nanoribbon and heterostructure, which includes a vacuum region that put a distance larger than 18 Å between the repeating images in the neighboring cells, whose Brillouin zones were sampled [29] by $21 \times 1 \times 1$ (nanoribbons) or $21 \times 2 \times 1$ (heterostructures) \mathbf{k} -point meshes. Geometry optimizations were performed by relaxing the ionic positions until the residual forces on atoms were reduced to be smaller than 0.01 eV/Å. *Ab initio* molecular dynamics (MD) simulations were performed at temperature 500 K with the aid of a Nosé-Hoover thermostat [30], integrating the equations of motion via the Verlet algorithm with a time step of 2 fs.

As will be discussed in Sec. III, we find that using a hybrid (HSE06) functional [31] (in lieu of a semilocal exchange-correlation functional) and/or the inclusion of spin-orbit coupling (SOC) in the calculation lead to relatively small variations in the electronic structure of 2D SL MoTe₂. We have thus chosen to work within the LSDA (without SOC) since the foregoing variations are *too small* to affect our conclusions in this paper.

III. 2D SL TRANSITION METAL DICHALCOGENIDES

Since composite structure of S_p/M_q and mM_p/M_q can be viewed as the periodically repeating stripes of the nanoribbons of constituents, the electronic structures of 2D constituents, MoTe₂, NiTe₂, and FeTe₂ are essential for our analysis. The calculated band structure of constituent 2D SL MoTe₂, NiTe₂, and FeTe₂ (or MX_2) will serve as references in this study.

In Fig. 1(a) the top and side views of the atomic structure of these 2D SL transition metal dichalcogenides are shown. A single layer consists of three atomic planes, where the planes of metal atoms are capped by the plane of chalcogen atoms from either side. The width of the single layer is denoted by Δ . The value of Δ is calculated to be 3.59 Å, 2.92 Å, and 3.08 Å for 2D SL MoTe₂, NiTe₂, and FeTe₂, respectively. The rectangular unit cell, which is suitable for the present study of

composite structures has fundamental translation vectors \mathbf{a} and \mathbf{b} . The values of optimized lattice constants are $a = 3.46$ Å and $b = 6.0$ Å for MoTe₂, $a = 3.59$ Å and $b = 6.22$ Å for NiTe₂, and $a = 3.48$ Å and $b = 6.02$ Å for FeTe₂. One-fourth of the corresponding Brillouin zone with symmetry directions are also shown. The cohesive energy per formula unit is calculated from the expression $E_c[2D-MX_2] = E_T[M] + 2E_T[X] - E_T[2D-MX_2]$ in terms of the total energies of free transition metal atom M, and chalcogen atom X, and the optimized total energy of MX_2 . Accordingly, the cohesive energies of MoTe₂, NiTe₂, and FeTe₂ are 15.64 eV, 12.98 eV, and 13.26 eV, respectively. The formation energy of a 2D SL MX_2 at $T = 0$ K relative to the parent three-dimensional (3D) bulk crystals, is $E_f[2D-MX_2] = E_c[3D-MX_2] - E_c[2D-MX_2]$. Three-dimensional bulk crystals of MX_2 are layered structures, where the interlayer attractive interaction is dominated by weak van der Waals interaction. Therefore, the formation energies of MoTe₂, NiTe₂, and FeTe₂ at $T = 0$ K are small, but negative. While $E_c > 0$ indicates cohesion relative to free atoms, $E_f < 0$ implies that 2D SL MX_2 corresponds to local minimum on the Born-Oppenheimer surface. The stability of these 2D, SL structures were demonstrated earlier theoretically [8].

Two-dimensional MoTe₂ is a stable nonmagnetic semiconductor with the direct fundamental band gap of $E_g = 1.25$ eV occurring along the Γ -X direction. The hybrid functional method [31] is applied to correct the electronic band structure, whereby the fundamental band gap increased only by 0.09 eV. Earlier studies on 2D SL transition metal dichalcogenides, in particular on MoS₂, showed that their electronic structures can be predicted successfully by LSDA. Since corrections by hybrid functional is small, but is time consuming for composite systems comprising several atoms, we carried out only LSDA calculations on optimized structure in the rest of the paper. When spin orbit coupling included the degenerate bands at the top of the valence band split only by ~ 0.2 eV. As for the other 2D constituents, 2D NiTe₂ is a nonmagnetic metal, but 2D FeTe₂ is a magnetic metal.

IV. COMMENSURATE COMPOSITE STRUCTURES OF TRANSITION METAL DICHALCOGENIDES

In this section we will treat periodic and finite-size composite structures of transition metal dichalcogenide MX_2 stripes

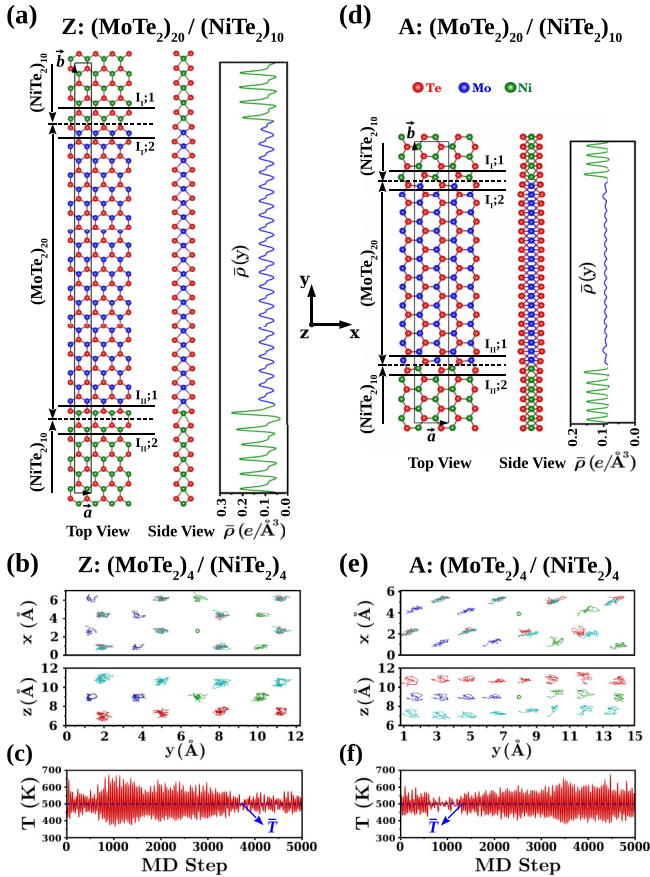


FIG. 2. (a) Top and side views of atomistic model of SL, in-plane composite structures $Z: S_p/M_q$ with $p = 20$, $q = 10$. The 2D rectangular unit cell with Bravais lattice vectors \mathbf{a} and \mathbf{b} is delineated by thin lines. Two types of boundaries having zigzag edge geometry between NiTe_2 and MoTe_2 stripes are indicated by I_I and I_{II} . The (x, z) -plane averaged self-consistent charge density $\bar{\rho}(y)$ corresponds to the optimized structure. (b) Trajectories of atoms $Z: S_p/M_q$ in the (x, y) and (z, y) planes attained from the average position of atoms in each 100 steps in the course of *ab initio* MD iterations at $T = 500$ K. (c) Variation of the temperature T and average temperature \bar{T} versus MD steps running at $T = 500$ K. (d)–(f) Same for $A: S_4/M_4$.

commensurately joined along their zigzag or armchair edges. We start by describing our atomistic model and examining the stability of the foregoing composite structures against thermal excitations.

TABLE I. Calculated values of the local strain ε (in %) at different regions (as indicated in the first row) of two composite structures A: and $Z: S_{20}/M_{10}$ with $S = \text{MoTe}_2$ and $M = \text{NiTe}_2$. Strain values are deduced from changes of bond lengths $d_{X-\text{Te}}$ ($X = \text{Mo}, \text{Ni}$ or Te) relative to those of parent 2D SL constituents.

		Center of S	Center of M	I_I (S side)	I_I (M side)	I_{II} (S side)	I_{II} (M side)
A: S_{20}/M_{10}	$d_{\text{Mo}-\text{Te}}$	0.4	–	1.0	–	1.7	–
	$d_{\text{Ni}-\text{Te}}$	–	–0.7	–	7.4	–	1.8
	$d_{\text{Te}-\text{Te}}$	0.8	1.4	5.7	5.8	5.6	6.0
Z: S_{20}/M_{10}	$d_{\text{Mo}-\text{Te}}$	0.3	–	0.5	–	–1.1	–
	$d_{\text{Ni}-\text{Te}}$	–	–0.6	–	–3.1	–	2.4
	$d_{\text{Te}-\text{Te}}$	–0.1	1.6	–6.0	2.8	–6.2	–1.3

A. Atomistic model and the stability

The atomistic model of the composite structure of S_p/M_q with two asymmetric boundaries, I_I and I_{II} along their zigzag and armchair boundaries, are shown in Figs. 2(a) and 2(d), respectively. Along the x direction the heterostructure extends to infinity (without any edge) in terms of stripes of MoTe_2 and NiTe_2 or NiTe_2 and FeTe_2 . The y direction is perpendicular to zigzag or armchair boundaries, along which the stripes of constituents repeat periodically. Hence, the 2D structure consisting of three parallel atomic planes, where the plane of metal atoms is capped by two Te atomic planes, has a 2D rectangular lattice, with lattice constants $\mathbf{a} \parallel \mathbf{x}$ and $\mathbf{b} \parallel \mathbf{y}$. Here one should note the dramatic differences in dimensionality between the present in-plane heterostructure and the well-known bulk heterostructures [32,33] or the heterostructures between different van der Waals solids [11]. In the latter systems, the interface are planar; electrons in metallic interfaces exhibit a 2D quantization with staircaselike density of states in terms of jumps of $m^*/\pi\hbar^2$ per unit area. Whereas in the present in-plane heterostructures the interface is 1D and metallic electrons at the interface display a density of states inversely proportional to the square root of energy, $1/\sqrt{E}$. $A: m M_p/M_q$ composite can be described by replacing Mo atoms with Fe atoms in Fig. 2(d).

Small lattice mismatches, $\Delta a/a \sim 0.03$, induce small strains in MoTe_2 , NiTe_2 stripes. For A: and $Z: S_p/M_q$ composites with large p and q the strain ε induced by the lattice mismatch is inhomogeneous, and hence attains different values in different regions of the composite structure. In Table I we present the calculated strain values for A: and $Z: S_{20}/M_{10}$.

The values in Table I indicate that the center of S stripes is usually under tensile strain, whereas M stripes are under compressive strain. Induced strains at the boundary regions are asymmetric and complex. We should address the questions of whether the in-plane composite can grow and remain stable despite the small lattice mismatch and inhomogeneous strain induced therefrom. To this end, we first calculate cohesive energies relative to free atoms, formation energies relative to 2D SL constituents, and also formation energies relative to nanoribbons E_{jf} . In Table II, the values calculated for periodic and finite-size composites are presented.

All composite structures have positive cohesive energy relative to free atom energies. On the other hand, the formation energies relative to 2D SL constituents have negative values. Their magnitudes are small for periodic composite structures, but become large for finite-size junctions because of free edges

TABLE II. The calculated values of the average cohesive energy \bar{E}_C (eV per pair), the formation energy E_f per cell at $T = 0$ K relative to 2D SL constituents (eV per cell), and the junction formation energy E_{jf} at $T = 0$ K relative to the corresponding nanoribbons (eV per cell).

System	\bar{E}_C	E_f	E_{jf}
A: S_2/M_2	14.01	-1.35	
A: S_2/M_{10}	13.39	-1.19	
A: S_{10}/M_2	15.12	-1.14	
A: S_{10}/M_{10}	14.29	-1.11	5.39
A: S_{20}/M_2	15.35	-1.33	
A: S_{20}/M_6	15.01	-1.01	
A: S_{20}/M_{10}	14.74	-1.26	5.26
Z: S_2/M_2	14.21	-0.55	
Z: S_2/M_{10}	13.44	-0.59	
Z: S_{10}/M_2	15.14	-0.91	
Z: S_{10}/M_{10}	14.31	-0.73	4.31
Z: S_{20}/M_2	15.36	-1.10	
Z: S_{20}/M_6	15.02	-0.66	
Z: S_{20}/M_{10}	14.75	-0.89	4.15
A: $M_2 - S_{10} - M_2$	14.73	-2.43	
A: $M_6 - S_{10} - M_6$	14.07	-3.59	
A: $M_{10} - S_{10} - M_{10}$	12.58	-3.72	4.65
A: $S_{10} - M_{10}$	14.14	-4.19	1.46
A: $S_{20} - M_{20}$	14.24	-4.34	3.06
Z: $M_2 - S_{10} - M_2$	14.75	-2.08	
Z: $M_6 - S_{10} - M_6$	14.15	-1.72	
Z: $M_{10} - S_{10} - M_{10}$	12.64	-1.75	4.29
Z: $S_{10} - M_{10}$	14.24	-2.19	2.85

adjacent to vacuums. Negative formation energies indicate that formation of composite systems unfavorable relative to 2D bare constituents. Under these circumstances, can composite structures form (grow) despite the negative formation energy? This question is answered by the calculations of junction formation energy. Here, the energies of two free standing stripes (nanoribbons) are compared with the energy of the composite formed from these stripes. The junction formation energies E_{jf} of periodic and finite composite structures are positive in Table II. Accordingly, the growth of a composite is favorable energetically, if one type (say M) of stripe continues to grow commensurately after the formation (or growth) of the other type (say S) of stripe.

As for the question of whether a composite structure corresponds to a local minimum and remains stable under strain, it can be answered by the analysis of dynamical and thermal stability. In the dynamical stability, positive frequencies of all modes should be ensured at $T = 0$ K. This, however, does not ensure that the given composite structure corresponds to a deep minimum, and hence sustains thermal excitations. In this respect, the thermal stability can be more critical. In this study, the stability of a composite structure is tested by finite-temperature *ab initio* MD simulations. After all, a structure which is dynamically unstable, becomes also unstable at low temperature MD simulations.

Results of our thermal stability tests on composite structures are summarized in Figs. 2(b) and 2(e), where the trajectories of atoms of Z: and A: S_4/M_4 heterostructures in the (y, x)

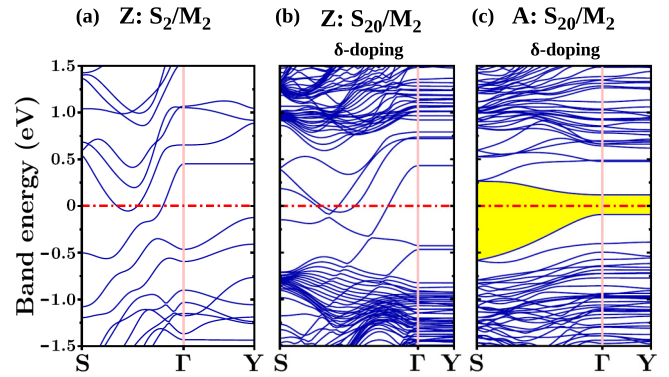


FIG. 3. Energy bands of specific composite structures. (a) Z: S_2/M_2 , a line compound of MoTe_2 and NiTe_2 , showing a metallic state. (b) Z: S_{20}/M_2 , stripes of semiconducting $(\text{MoTe}_2)_{20}$ which are δ doped by narrow metallic $(\text{NiTe}_2)_2$ stripes along their zigzag edges. Metallic bands are localized in the M stripe. (c) A: S_{20}/M_2 , in which stripes of semiconducting $(\text{MoTe}_2)_{20}$ are δ doped by narrow metallic $(\text{NiTe}_2)_2$ stripes along their armchair edges is a narrow band gap semiconductor.

and (y, z) planes are shown. These trajectories are obtained from the position of atoms (averaged over every 100 MD steps) in the course of MD iterations. The fluctuations and average of temperatures throughout 5000 steps are also shown in Figs. 2(c) and 2(f), respectively. The tendency of the atoms to restore their equilibrium positions at a temperature (500 K) considerably higher than room temperature indicates that the in-plane heterostructures are stable and can sustain applications at room temperature.

B. $\text{MoTe}_2/\text{NiTe}_2$ composite structures

We now focus on the electronic structure of A: and Z: S_p/M_q composite structures. Our results are summarized by the energy bands presented in Fig. 3. Composite structures (or line compounds) Z: S_2/M_2 and A: S_2/M_2 are metals. The situation with $p = 2$, but large q or vice versa can be viewed as if one of the 2D constituent is δ doped by the other along the x direction. For example, δ doping of the wide semiconducting MoTe_2 stripe by the narrow metallic NiTe_2 stripe, which are commensurately joined along their zigzag edges is modeled by Z: S_{20}/M_2 . Even if the resulting composite structure is seemingly metallic in momentum space, the metallic states are confined to the narrow NiTe_2 stripe. The wide MoTe_2 stripes continue to be semiconducting. Energy bands projected to the bonds in the unit cell demonstrate that the metallic bands occurring in the band gap of MoTe_2 are actually separated from the semiconducting stripe and display a 1D character having the density of states $D(E) \sim 1/\sqrt{E}$. Conversely, the same δ -doped composite with the A boundary, namely A: S_{20}/M_2 is a narrow band gap semiconductor in Fig. 3, where even the narrow M stripe has a narrow band gap. This difference between Z and A edges is explained by the fact that the M stripes of the armchair edged composite is narrower than the Z-edged ones even if they have the same value of q . However, the narrow band gap is closed by increasing the width of the M stripe. For example, A: S_{20}/M_6 is metallized. Metallic NiTe_2 lines can be considered as *interconnect* in MoTe_2 -based nanoelectronics.

On the other hand, wide M stripes δ doped by narrow S stripes, namely $Z:S_2/M_{20}$ and $A:S_2/M_{20}$ continue to be metallic.

For both small p and q , the composites display properties different from constituent 2D compounds. However, as the S or M stripe is widened with increasing p or q , the properties of wide stripes approach those of respective parent 2D constituents, except the boundary region. Under this circumstance, electronic states are confined to either one of these stripes to construct periodically repeating metal-semiconductor junctions. Briefly, p and q function as parameters to design in-plane composite nanostructures with diverse electronic properties. Under the lateral electric field perpendicular to the boundary of a finite-size composite, A : or $Z:M_q - S_p - M_q$, metallic stripes at either side of the insulating stripe are charged with opposite polarity and hence store energy. This system operates as an *in-plane* nanocapacitor [22], and can be viewed as a critical element in atomically thin circuits [21]. As discussed in forthcoming sections, in the similar finite-size composite, the band gap of the S_p stripe acts as a tunneling barrier with well-defined barrier height between two adjacent M_q . Also, the combination $M - S - M$ units can operate as a double barrier resonant tunneling device.

C. $\text{MoTe}_2/\text{NiTe}_2$ heterostructure: Schottky barrier

Having outlined critical features of the composite structures, let us focus now on the in-plane, periodic heterostructures with large p and q , for example, $Z:S_{20}/M_{10}$. Despite significant deformations at the I_I boundary and the formation energy relative to constituent nanoribbons is $E_{jf} = 4.15$ eV per cell, the formation of junctions of individual constituent nanoribbons or S and M stripes is favored. Once the ribbons are joined commensurately, *space-charge regions* form at the boundaries as demonstrated in Fig. 4 and determine the bending and lineup of band edges in compliance with the models proposed earlier [34], depending on whether charged impurities are located near I_I and I_{II} .

In the absence of charged impurities as in the present study the bending has to be linear [34]. In $Z:S_{20}/M_{10}$, Schottky barriers develop in compliance with Fig. 4(a). The (z,x) plane averaged potential $\bar{V}(y)$ and the macroscopic average potential [35] $V_{\text{macro}}(y)$ show changes of potential at the boundaries, and also indicate an asymmetry between two different types of boundaries, I_I and I_{II} . The variation of the band gap in direct space, thus the occurrence of alternating metallic and semiconducting zones along the y direction, is revealed by the densities of states projected to Mo-Te and Ni-Te bonds located at different positions of the unit cell (LDOS) as shown in the insets of Fig. 5(a). While LDOS in the MoTe_2 stripe has a band gap of 1.25 eV, it is metallic in the NiTe_2 stripe; the Fermi level is pinned by high density of states located near the center of the band gap at I_{II} .

This information is, however, absent in the band structure of $Z:S_{20}/M_{10}$ in momentum space, which displays a metallic state. Separation of semiconducting and metallic regions can also be revealed by the analysis of the contributions of different Mo-Te and Ni-Te bonds in the different band states of the whole heterostructure. While several bands cross the Fermi level in the first panel of Fig. 5(c), in the second panel the contribution of a Mo-Te bond to the bands is absent in the gap.

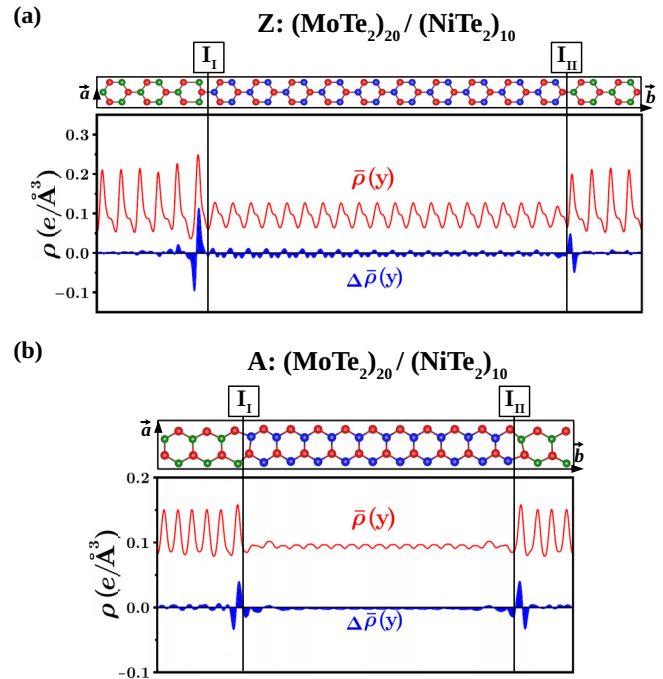


FIG. 4. The (z,x) plane averaged charge density $\bar{\rho}(y)$ and charge transfer $\Delta\bar{\rho}(y)$ in $Z:S_{20}/M_{10}$ (a) and in $A:S_{20}/M_{10}$ (b). $\Delta\bar{\rho}(y)$ is computed by subtracting the sum of charge densities of 2D SL MoTe_2 and 2D SL NiTe_2 from the charge density of the heterostructure. The upper panels show optimized atomic configurations of each composite structure with two boundaries I_I and I_{II} . The blue (green) and red balls represent Mo (Ni) and Te atoms, respectively. The total charge transfer at the boundaries is $-0.8e$ and $-1.1e$ in $Z:S_{20}/M_{10}$ and $A:S_{20}/M_{10}$, respectively.

This means that while the states in the MoTe_2 -region stripe develop an energy gap, the metallic states of the NiTe_2 region with energy coinciding with this gap cannot propagate in the MoTe_2 region; rather they decay and slightly penetrate to it. This situation is characteristic of a *metal-insulator transition* in a 2D metallic system. Notably, specific NiTe_2 states, which can match to the momentum and energy of MoTe_2 states in the valence and conduction band continua can propagate along k_y without confinement.

In view of the earlier theories [35] we calculated the energy position and the Schottky barrier height. To this end, we first determined energies of E_{CB} and E_{VB} of 2D SL MoTe_2 from its $V_{\text{macro}}(y)$. We marked these energies in Fig. 5(a) from the calculated $V_{\text{macro}}(y)$ fixing the conduction and valence band edges. This way, the linear variation of $V_{\text{macro}}(y)$ at the boundaries is reflected to linear band bending. Notably, the energies of the band edges in the direct space in Fig. 5(a) are in fair agreement with the edges deduced from the edges in LDOS calculated at Mo-Te bonds in the S stripe. At the end the Schottky barrier energies are found to be $E_S = 1.03$ and 1.07 eV (for I_I and I_{II} , respectively) for $Z:S_{20}/M_{10}$ in Fig. 5. Because of asymmetry of the charge transfer across I_I and I_{II} boundaries, a small tilt of band edges, due to the tilt of $V_{\text{macro}}(y)$, is noticed.

As seen in Figs. 6(a)–6(c), Schottky junctions form also at the boundaries of $A:S_{20}/M_{10}$. In contrast to the Z -type

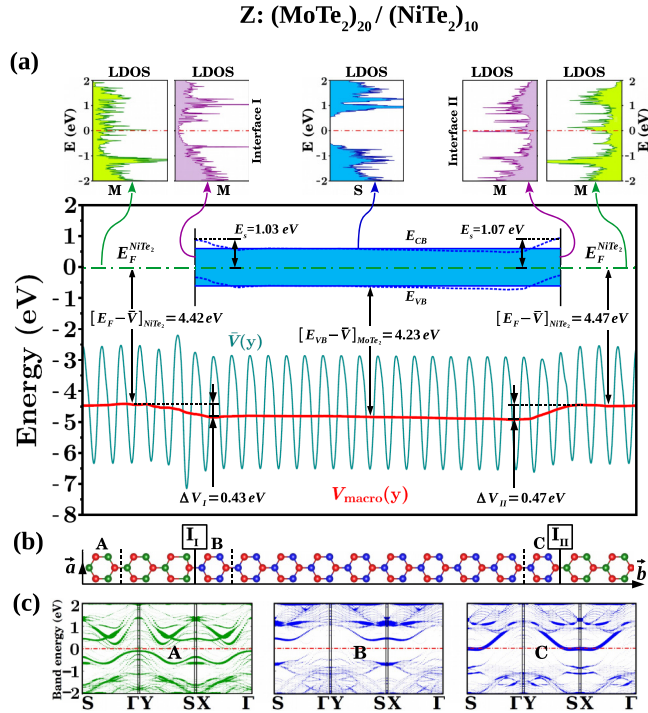


FIG. 5. Z:(MoTe₂)₂₀/(NiTe₂)₁₀ (or Z:S₂₀/M₁₀) heterostructure. (a) The (z,x) plane averaged potential $\bar{V}(y)$ (in turquoise) and the macroscopic average potential $V_{\text{macro}}(y)$ (in red). The alignment and bending of VB and CB edge energies with respect to the Fermi level E_F (marked by the dash-dotted line) is shown. The Schottky barrier height E_S relative to E_F is depicted. The local densities of states (LDOS) in the vicinity of E_F are shown at metallic (M), semiconducting (S), and boundary regions by insets. (b) Optimized atomic configuration of Z:S₂₀/M₁₀ is described by blue (green) and red balls representing Mo (Ni) and Te atoms, respectively. **a** and **b** are the lattice translation vectors of the 2D rectangular cell of the heterostructure. (c) Energy bands weighted by the contribution of particular bonds designated in (b) by A, B, and C. Thicker bands denote higher contribution.

boundary, the potential profiles, viz. $V_{\text{macro}}(y)$, at I_I and I_{II} [cf. Fig. 6(a)] are virtually identical in the A-type boundary. Thus the Schottky barrier height is estimated to be $E_S = 1.12$ eV for both I_I and I_{II} in A:S₂₀/M₁₀.

The band structures and the isosurfaces of charge densities $\rho_{nk}(\mathbf{r}) = \Psi_{nk}^*(\mathbf{r})\Psi_{nk}(\mathbf{r})$ of specific states indicated by A, B, C, D, and E therein are presented in Fig. 7. Despite the fact that several bands seemingly cross the Fermi level in \mathbf{k} space and hence imply a metallic state, the charge density plots confirm the confinement of specific states as discussed above. States of energy bands $E_n(\mathbf{k})$ in the gap region are confined to NiTe₂ stripes and to the boundaries. In Fig. 7(a), the isosurfaces of the states A and B in the valence and conduction band edge are confined to the *S* stripe. In contrast, specific states in the gap are confined to the *M* stripe. The charge density isosurfaces of the states C and D deserve special attention. These states form the bands in the gap, which have high dispersion along the Γ -X direction parallel to the stripes. The minimum of the band of C is above the Fermi level and corresponding states are localized at the boundary I_I , mainly at the Mo-Te bond. The band states D is also highly dispersive along k_x , but is localized strongly

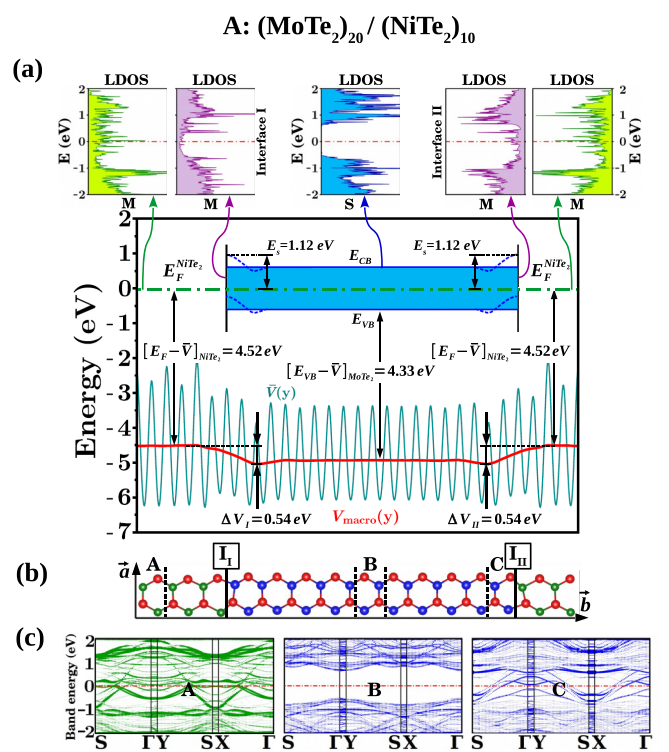


FIG. 6. A:(MoTe₂)₂₀/(NiTe₂)₁₀ (or A:S₂₀/M₁₀) heterostructure. (a) The (z,x) plane averaged potential $\bar{V}(y)$ (in turquoise) and the macroscopic average potential $V_{\text{macro}}(y)$ (in red). The alignment and bending of VB and CB edge energies with respect to the Fermi level E_F (marked by the dash-dotted line) is shown. The Schottky barrier height E_S relative to E_F is depicted. The local density of states (LDOS) in the vicinity of E_F is shown at metallic *M*, semiconducting *S*, and boundary regions in the insets. (b) Optimized atomic configurations of A:S₂₀/M₁₀ is described by blue (green) and red balls representing Mo (Ni) and Te atoms, respectively. **a** and **b** are the lattice translation vectors of the 2D rectangular cell of the heterostructure. (c) Energy bands weighted by the contribution of particular atoms indicated in (b) by A, B, and C.

along the *y* axis at the boundary I_{II} , mainly at Mo-Te bonds; the Fermi level is pinned by this band. Both C and D states are reminiscent of the interface or metal-induced gap states [33,36,37] in 3D metal-semiconductor junctions. Here, these states are, however, strictly 1D metallic states in a strictly 2D SL system.

In Fig. 7(b), the A:(MoTe₂)₂₀/(NiTe₂)₁₀ in-plane heterostructure exhibits similar behaviors. The A and B states at the edges of CB and VB of the semiconducting MoTe₂ stripe are confined to this region. The C state of the dispersive bands in the band gap is confined to the boundaries I_I and I_{II} and is strictly one-dimensional. The band state indicated by D originates from NiTe₂ stripes and is 2D for large *q*.

D. Single metal-semiconductor junction and tunneling barrier

In a finite system consisting of one *S* stripe joined *M* stripe, for example, Z:M₁₀ – S₁₀, one can attain a 1D metal-semiconductor junction with a single Schottky barrier as shown in Fig. 8. This system appears as a single stripe composed of *S* and *M* stripes and capped by vacuum from

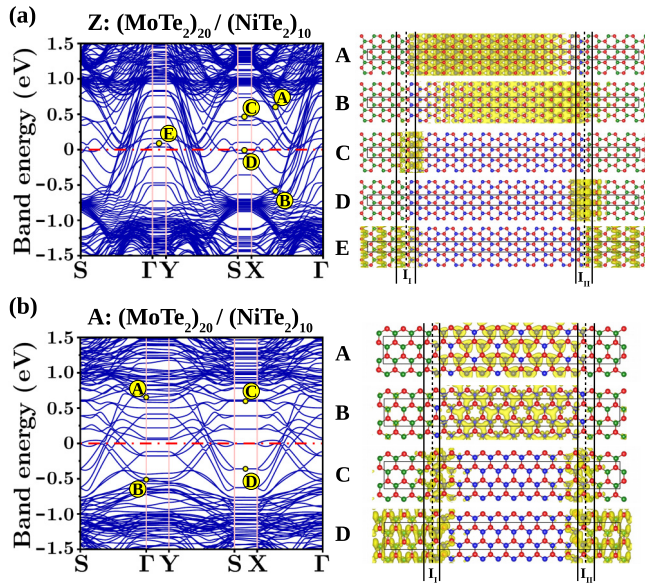


FIG. 7. (a) (Left) Energy band structure of $Z:S_{20}/M_{10}$ in momentum space. (Right) Isosurfaces of charge densities of the selected band states A, B, C, D, and E. The isosurface charge density is $0.0005 e/\text{\AA}^3$. (b) Same for $A:S_{20}/M_{10}$.

both sides. The optimized atomic configuration is presented in Fig. 8(a). Specific regions of interest are indicated by numerals 1–6. The bands contributed by the bonds in regions 1–3 in the NiTe₂ stripe cross the Fermi level and hence attribute a metallic state. In contrast, in regions 5 and 6 in the MoTe₂

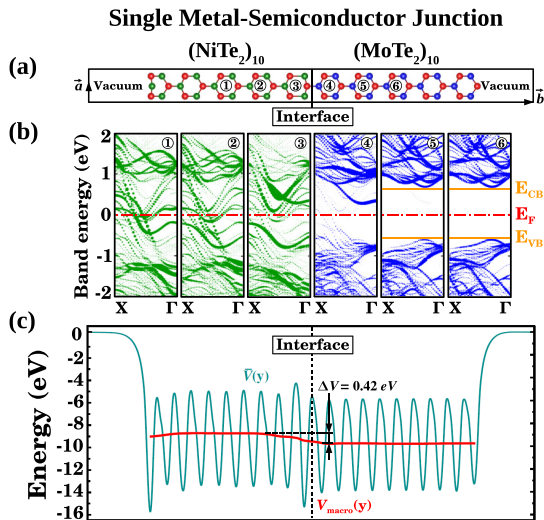


FIG. 8. A (finite-size) single metal-semiconductor junction $Z:(\text{NiTe}_2)_{10} - (\text{MoTe}_2)_{10}$. (a) The atomic configuration and vacuum space at both sides. Numerals indicate specific regions and Mo-Te or Ni-Te bonds in the junction. (b) Contributions of specific regions are indicated by numerals in (a) to the energy bands. Thicker bands denote higher contribution. Bands are metallic at the NiTe₂ side, but a gap is opened in the MoTe₂ side. In panels 5 and 6 no states exist between E_{CB} and E_{VB} . (c) (xz) plane averaged electronic potential and its average $V_{macro}(y)$.

stripe a band gap is opened indicating a semiconducting state. The common Fermi level is located almost at the middle of the gap. This finite-size system mimics a single Schottky barrier despite the unsaturated bonds at either edge facing the vacuum. Plane averaged potential $\bar{V}(y)$ shows differences at the edges. The edge effects can be eliminated through the saturation by specific atoms. The level of average potential shifts down by 0.42 eV at the semiconducting side.

A tunneling barrier is constructed by commensurately joined $(\text{NiTe}_2)_{10} - (\text{MoTe}_2)_{10} - (\text{NiTe}_2)_{10}$ (or $M_q - S_p - M_q$) stripes capped by vacuum from both sides. While NiTe₂ stripes remain metallic, a gap opens in the MoTe₂ stripe in between. Metallic states see the edge of the conduction band of the semiconducting stripe, which is aligned 1.1 eV above the Fermi level as a tunneling barrier of $\Phi_B = 1.1 eV$. As a result metallic states cannot propagate in the semiconducting stripe, but they can tunnel from the left side to the right side. The width w and height Φ_B of the barrier can be tuned by the width of MoTe₂ or by p . For $p = 2$, Φ_B does not occur, and is considered as a δ doping. However for $p \geq 5$ a well-defined barrier of significant width starts to form.

The above combination of S and M stripes can also function as an in-plane nanocapacitor. When the charges of opposite polarity accumulate in different M stripes having the S stripe of appropriate width, a lateral electric field \vec{E} between M stripes across the S stripe is induced. Conversely, a lateral electric field \vec{E} applied across the S stripe leads to the storage of the charge of different polarity in different M stripes. Such a system also can store energy. Earlier, an in-plane nanocapacitor constructed from graphene/h-BN/graphene stripes was shown to attain high capacitance value comparable to those of supercapacitors [22].

A resonant tunneling double barrier (RTDB) device can be constructed by the extension of the tunneling barrier in Fig. 9(d) through the combination $M_q - S_p - S'_t - S_p - M_q$, where S'_t is as shown in Fig. 9(e). Here S'_t is an SL MX_2 stripe having narrow band gap and nearly lattice matched to the S stripe. Trigonal NiSe₂, hexagonal WTe₂ or CrTe₂ fit to these descriptions [8] and form a quantum well between two S stripes. Confined electronic states in this well mediate very fast tunneling time from the left M stripe to the right M stripe. The character of this device can be determined by S' , t , and p .

E. $(\text{FeTe}_2)_t / (\text{NiTe}_2)_q$ heterostructure: a spin valve

Finally, we discuss a composite constructed from magnetic and nonmagnetic transition metal dichalcogenides, $(\text{FeTe}_2)_t / (\text{NiTe}_2)_q$ described in Fig. 10. For large enough t and q , the magnetic state indigenous to 2D FeTe₂ appears to be confined in its respective stripe with the breakdown of spin degeneracy. At the end, $A:mM_{10}/M_q$ composite acquires a permanent magnetic moment localized in the FeTe₂ stripe, which, in turn, displays a half metallic state; namely spin-up bands are metallic, while spin-down states become semiconducting with a band gap of $\sim 0.2 eV$. In contrast, the adjacent NiTe₂ stripes continue to be nonmagnetic metal with spin-degenerate bands and diminishing magnetic moment. Such a system can operate as a spin valve in the combination, $M_q - mM_t - M_q$. The situation at the boundaries I_I and I_{II} are crucial because of the diffusion of spin states to nonmagnetic metal and

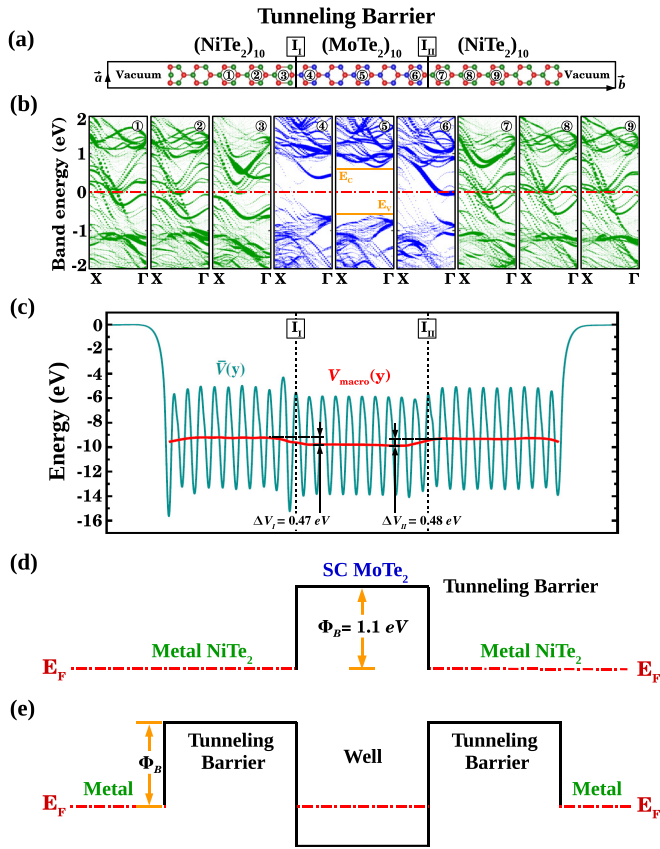


FIG. 9. $(\text{NiTe}_2)_{10} - (\text{MoTe}_2)_{10} - (\text{NiTe}_2)_{10}$ (or $M_q - S_p - M_q$) junction functioning as a tunneling barrier between two metal electrodes also as a nanocapacitor. (a) The optimized atomic configuration with boundaries I_I and I_{II} . Numerals indicate specific regions and Mo-Te or Ni-Te bonds. (b) Contributions of specific regions indicated by numerals in (a) to the energy bands. Thicker bands denote higher contribution. Bands are metallic at the NiTe_2 side, but a gap is opened in the MoTe_2 side. (c) (xz) plane averaged electronic potential $\bar{V}(y)$, and its average $V_{\text{macro}}(y)$. (d) Schematic description of the tunneling barrier with barrier energy Φ_B between two metals at both sides. (e) Formation of resonant tunneling double barrier RTDB structure with $M_q - S_p - S'_i - S_p - M_q$, where S'_i denotes hexagonal or trigonal SL transition metal dichalcogenides stripe with narrow band gap.

deserves an extensive study. As for $Z:mM_{10}/M_q$ composite heterostructure, it is magnetic metal in the FeTe_2 stripe, but the magnetism disappears in the NiTe_2 stripe.

V. CONCLUSION

In conclusion, single-layer, in-plane junctions of MoTe_2 , NiTe_2 , and FeTe_2 stripes along zigzag or armchair edges can construct periodically repeating or finite-size commensurate composite structures. We showed that they can constitute a new class of materials with a very wide range of features and functionalities, such as 2D metallic or narrow band gap semiconducting compounds, narrow 1D metallic interconnects or nanowires in a wide 2D semiconductor sheet, tunneling barriers and resonant tunneling double barrier structures, nanocapacitor, single and periodic metal-semiconductor junctions forming Schottky barrier, and nonmagnetic metal/half

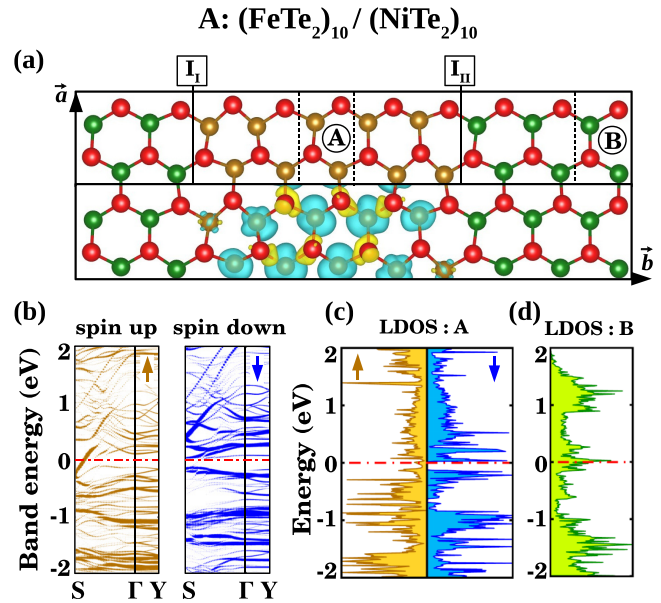


FIG. 10. $A:(\text{FeTe}_2)_{10}/(\text{NiTe}_2)_{10}$, armchair edged, magnetic-nonmagnetic metal composite structure. (a) Atomic configurations with Fe, Ni, and Te atoms are described by gold, green and red balls, respectively. A and B regions comprising specific Fe-Te and Ni-Te bonds and local magnetic moment isosurfaces are also shown. (b) Contributions of atoms (or bonds) at the A region to the spin-up and spin-down bands in the momentum space. Thick lines indicate higher contribution to the given band. (c) LDOS showing that spin-down states at the center of the FeTe_2 stripe in the A region display a band gap of ~ 0.2 eV, while spin-down states have a metallic density. (d) Spin degenerate LDOS at the center of the NiTe_2 stripe in the B region. The zero of energy is set to the Fermi level of the whole composite.

metal heterostructures with spin-valve effect. These features can be controlled by the type and width of the stripes of single-layer transition metal dichalcogenides and can be exploited in various device applications.

Fundamental features revealed in these composites, such as metal-insulator transitions, nonmagnetic-magnetic metal phase separation, formation of strictly 1D states in a 2D system, are interesting and able to initiate further research. In-plane heterostructures constructed by nearly lattice matched semiconducting stripes of different band gaps, such as MoTe_2 and CrTe_2 (also trigonal NiSe_2), can form multiple quantum well structures. Beyond the stripe structure, one can also consider single or periodic core/shell structures. In the latter metallic or semiconducting domains of selected geometry and shape can be embedded commensurately in a single-layer, 2D semiconductor to form regular arrays of the mesh of quantum dots.

ACKNOWLEDGMENTS

The numerical calculations reported here were carried out at the High Performance and Grid Computing Center (TRUBA Resources) of TUBITAK ULAKBIM. S.C. acknowledges financial support from the Academy of Sciences of Turkey (TÜBA).

- [1] P. Joensen, R. Frindt, and S. Morrison, *Mater. Res. Bull.* **21**, 457 (1986).
- [2] K. S. Novoselov *et al.*, *Proc. Natl. Acad. Sci. (USA)* **102**, 10451 (2005).
- [3] B. Hinnemann *et al.*, *J. Am. Chem. Soc.* **127**, 5308 (2005).
- [4] K. F. Mak, C. Lee, J. Hone, J. Shan, and T. F. Heinz, *Phys. Rev. Lett.* **105**, 136805 (2010).
- [5] A. Splendiani *et al.*, *Nano Lett.* **10**, 1271 (2010).
- [6] B. Radisavljevic *et al.*, *Nature Nanotechnol.* **6**, 147 (2011).
- [7] C. Ataca *et al.*, *J. Phys. Chem. C* **115**, 3934 (2011); C. Ataca and S. Ciraci, *ibid.* **115**, 13303 (2011); C. Ataca *et al.*, *ibid.* **115**, 16354 (2011); C. Ataca and S. Ciraci, *Phys. Rev. B* **85**, 195410 (2012).
- [8] C. Ataca, H. Şahin, and S. Ciraci, *J. Phys. Chem. C* **116**, 8983 (2012).
- [9] H. Sevinçli, M. Topsakal, and S. Ciraci, *Phys. Rev. B* **78**, 245402 (2008).
- [10] H. Şahin, S. Cahangirov, M. Topsakal, E. Bekaroglu, E. Akturk, R. T. Senger, and S. Ciraci, *Phys. Rev. B* **80**, 155453 (2009).
- [11] A. K. Geim and I. V. Grigorieva, *Nature (London)* **499**, 419 (2013).
- [12] A. D. Bartolomeo, *Phys. Rep.* **606**, 1 (2016).
- [13] Z. Liu *et al.*, *Nature Nanotechnol.* **8**, 119 (2013); Y. Gong *et al.*, *Nat. Mater.* **13**, 1135 (2014).
- [14] X. Hong *et al.*, *Nature Nanotechnol.* **9**, 682 (2014).
- [15] H. Lim *et al.*, *Chem. Mater.* **26**, 4891 (2014).
- [16] R. T. Tung, *Appl. Phys. Rev.* **1**, 011304 (2014).
- [17] J. N. Coleman *et al.*, *Science* **331**, 568 (2011).
- [18] Z. Liu *et al.*, *J. Phys. Soc. Jpn.* **84**, 121005 (2015).
- [19] Y. Katagiri, T. Nakamura, A. Ishii, C. Ohata, M. Hasegawa, S. Katsumoto, T. Cusati, A. Fortunelli, G. Iannaccone, G. Fiori, S. Roche, and J. Haruyama, *Nano Lett.* **16**, 3788 (2016).
- [20] Z. Liu *et al.*, *Nano Lett.* **11**, 2032 (2011).
- [21] M. P. Levendorf *et al.*, *Nature (London)* **488**, 627 (2012).
- [22] V. O. Özçelik and S. Ciraci, *J. Phys. Chem. C* **117**, 15327 (2013).
- [23] R. Drost *et al.*, *Nano Lett.* **14**, 5128 (2014).
- [24] V. O. Özçelik, E. Durgun, and S. Ciraci, *J. Phys. Chem. C* **119**, 13248 (2015).
- [25] G. Kresse and J. Furthmüller, *Phys. Rev. B* **54**, 11169 (1996).
- [26] D. M. Ceperley and B. J. Alder, *Phys. Rev. Lett.* **45**, 566 (1980); J. P. Perdew and A. Zunger, *Phys. Rev. B* **23**, 5048 (1981).
- [27] P. E. Blöchl, *Phys. Rev. B* **50**, 17953 (1994).
- [28] G. Kresse and D. Joubert, *Phys. Rev. B* **59**, 1758 (1999).
- [29] H. J. Monkhorst and J. D. Pack, *Phys. Rev. B* **13**, 5188 (1976).
- [30] S. Nose, *J. Chem. Phys.* **81**, 511 (1984).
- [31] J. Heyd, G. E. Scuseria, and M. Ernzerhof, *J. Chem. Phys.* **118**, 8207 (2003); A. V. Krukau, O. A. Vydrov, A. F. Izmaylov, and G. E. Scuseria, *ibid.* **125**, 224106 (2006).
- [32] L. Esaki and R. Tsu, *IBM J. Res. Dev.* **14**, 61 (1970).
- [33] H. Kroemer, *Proc. IEEE* **70**, 13 (1982).
- [34] W. Schottky, *Naturwissenschaften* **26**, 843 (1938); N. F. Mott, *Proc. Cambridge Philos. Soc.* **34**, 568 (1938); J. Bardeen, *Phys. Rev.* **71**, 717 (1947).
- [35] R. G. Dandrea, C. B. Duke, and A. Zunger, *J. Vac. Sci. Technol. B* **10** (1992); R. G. Dandrea and C. B. Duke, *J. Vac. Sci. Technol. A* **11** (1993).
- [36] V. Heine, *Phys. Rev.* **138**, A1689 (1965); J. Tersoff, *Phys. Rev. Lett.* **52**, 465 (1984).
- [37] S. Ciraci, A. Baratoff, and I. P. Batra, *Phys. Rev. B* **43**, 7046 (1991); I. Batra, E. Tekman, and S. Ciraci, *Prog. Surf. Sci.* **36**, 289 (1991).